Carbothermally Synthesized MoO_2 as an Insertion Host for High-Performance Li-ion Capacitors

Madhusoodhanan Lathika Divya,[1] Yun-Sung Lee,[2] and Vanchiappan Aravindan[1,*,†]

[1] *Department of Chemistry, Indian Institute of Science Education and Research (IISER), Tirupati 517507, India*
[2] *School of Chemical Engineering, Chonnam National University, Gwang-ju, 61186, Republic of Korea*

(Received 19 July 2022; revised 24 November 2022; accepted 30 January 2023; published 6 March 2023)

This work presents the possibility of considering MoO_2 nanorods synthesized by the carbothermal reduction of MoO_3 as an intercalation- or insertion-type anode for lithium-ion capacitor (LIC) assembly. The mechanism for Li intercalation into MoO_2 carbon composite (MoO_2-C) is studied in a half-cell assembly within the potential window of 0.8–3 V vs Li^+/Li. The material can deliver an initial discharge capacity of about 225–250 mAh g^{-1} with excellent cyclic stability over 500 galvanostatic charge-discharge cycles at a current density of 100 mA g^{-1}. Furthermore, the performance of MoO_2-C as a battery-type (intercalation) anode in LIC assembly is studied by pairing it with a commercial activated carbon (AC) cathode. The role of prelithiation and operating-voltage window on the electrochemical performance of AC//MoO_2-C LIC is analyzed. Such a LIC assembly without prelithiation, when tested within the voltage window of 1.7–3.2 V, can provide an energy density of about 75.27 Wh kg^{-1} and maintain about 70% of its initial capacity after 4500 cycles. Moreover, such a LIC prototype's low- and high-temperature performance is also evaluated. This study clearly shows the possibility of considering MoO_2-based LIC systems as a strong competitor for $Li_4Ti_5O_{12}$-based LIC assembly, providing much safer features than graphite-based LIC configurations.

DOI: 10.1103/PhysRevApplied.19.034016

I. INTRODUCTION

Lithium-ion capacitors (LICs) have risen in popularity among various electrochemical energy-storage systems, as they exhibit higher energy density than traditional supercapacitors (electrochemical double-layer capacitors, EDLCs) and higher power and cyclic stability than lithium-ion batteries (LIBs) [1]. LICs are also known as hybrid capacitors, as they effectively combine both EDLC and LIB technology [2–5]. Typically, they comprise one battery-type electrode as the anode and a capacitor-type electrode as the cathode. Activated carbon (AC) is usually used as a capacitor-type cathode for LIC assembly. At the same time, a battery-type anode works according to different faradaic reaction mechanisms, such as intercalation, conversion, or alloying [6,7]. Intercalation-type electrode materials display better stability than conversion- and alloying-type materials, and they exhibit layered structures with suitable intercalation potential to ensure safety and long-term stability [8–10]. Graphite is one of the most considered anodes for lithium- (Li) based energy-storage devices (LIBs and LICs), as it is of low cost, abundant, nontoxic, and structurally stable with a high theoretical capacity (∼372 mAh g^{-1}). However, its low operating potential (∼0.1 V vs Li^+/Li) is the root of Li dendrite formation, an undesirable side reaction during the charge-discharge process, which causes safety issues, mostly at high power rates [11–14]. Hence, there is a requirement for finding alternative anode materials for LIB and LIC applications. As an alternative to graphite, transition-metal oxides (TMOs) have been proposed by many researchers [15–18]. Conversion-based TMOs can store more Li atoms at relatively low potential (∼0.6–1 V vs Li^+/Li), but enormous polarization and capacity fading, due to significant volume changes, hinder their application, whereas the electrochemical intercalation of Li ions into TMOs has received substantial consideration in the last decade [19]. They can act as hosts for metal ions (mainly Li), owing to the possibility of different oxidation states. Moreover, intercalation is possible with three-dimensional framework, two-dimensional layered, and one-dimensional (1D) ribbon-type host structures [20].

Among TMOs, molybdenum oxide (MoO_x) is attractive for its unusual chemistry as a result of multiple valence states [21]. Molybdenum dioxide (MoO_2), a dichalcogenide, has received ample consideration as an active anode material for LIBs since 1980 [22–24]. Due to its high electronic conductivity, electrochemical activity, thermal and chemical stability, and rich electrochemistry

*aravind.van@gmail.com
†aravind_van@yahoo.com

associated with Mo, MoO_2 has gained substantial interest. In 1955, researchers reported the reduction of MoO_3 to six stable Magnli phases, ending at MoO_2, a lower stable oxide of Mo [25,26]. MoO_2 crystallizes in the monoclinic structure with space group $P21/c$, a distorted rutile structure with tetragonal orientation (metal-metal pairs along c direction), and having a coordination number of six in the case of metals and three for oxygen [25,27]. The mineralogical form is known as tugarinovite. MoO_6 octahedra linkages in the distorted rutile structure result in 1D channels along the a axis, where reversible insertion of Li ions can occur. Two different Li^+-ion-based charge-storage mechanisms in MoO_2 are reported: (i) Li^+-ion intercalation-deintercalation into or out of the MoO_2 host within the potential range of 1.0–3.0 V vs Li^+/Li (addition-type reaction), a one-electron reaction with a theoretical capacity of 210 mAh g^{-1} [Eq. (1)]; and (ii) a conversion reaction below 1.0 V vs Li^+/Li with a theoretical capacity of 630 mAh g^{-1} [Eq. (2)].

$$MoO_2 + Li^+ + e^- - \leftrightarrow LiMoO_2, \quad (1)$$

$$3Li^+ + 3e^- + LiMoO_2 \leftrightarrow Mo + 2Li_2O. \quad (2)$$

Most of the reported works on MoO_2 considered the combination of intercalation and conversion to attain high capacity [28–35]. However, the conversion reactions are kinetically slow, with a severe fading in capacity upon cycling due to high hysteresis and volume expansion [36]. However, few studies have been reported on the possible application of MoO_2 as an intercalation anode for Li-based charge-storage devices [37]. In 1987, Dahn *et al.* [22] reported the possibility of using MoO_2 as a reducing intercalation compound for secondary electrochemical cells. Eventually, in 2014, Sen *et al.* [37] conducted a thorough study on applying MoO_2 as an intercalation anode for LIB assembly. The study confirmed that there was a reversible multistep phase transformation from monoclinic MoO_2 to orthorhombic (Li_xMoO_2, $0.45 < x < 0.75$) to monoclinic ($LiMoO_2$) during the insertion and extraction of Li. Within the potential window of 1.0–2.2 V vs Li^+/Li, synthesized MoO_2 material (reduction of MoO_3 under a hydrogen atmosphere) can exhibit outstanding electrochemical stability over 200 charge-discharge cycles. Furthermore, Liu *et al.* [38] studied the intercalation behavior of MoO_2 nanoplates synthesized by the hydrothermal method and reported an initial discharge capacity of 251 mAh g^{-1} at 0.2 C rate, along with excellent power performance. Dunn's group [33] described the size-dependent electrochemical pseudocapacitive behavior of nanosized MoO_2. They stated that there was suppression of phase transformation in nanosized materials, which helped preserve ion-diffusion tunnels in monoclinic MoO_2 and provided better charge-storage kinetics than microsized MoO_2. The effect of MoO_2 particle size on Li-ion storage capacity was also reported by Kim *et al.* [39]. They explained that the increased capacity of nanoparticles was due to the increased electrolyte contact area of MoO_2 particles, resulting in a decreased diffusion path of Li ions into MoO_2 particles. Previous studies also show that nanoengineering of MoO_2 particles or making a composite with carbon can alter the Li-insertion capacity of MoO_2 particles [35,39]. Also, Zhang *et al.* [32] synthesized uniform MoO_2 nanoparticles that could deliver high capacity and extended cycle life when analyzed as an intercalation anode. Some discrepancies in the previous studies have to be explored in further research. Moreover, the suitability of an intercalation-based MoO_2 anode for LIC assembly has not been extensively studied, and only two reports are available in which the results are not comparable [29,32,40].

Here, MoO_2 nanoparticles are synthesized by the carbothermal reduction of commercial MoO_3, and we characterize the physical and morphological properties of the material. The Li-intercalation property of the material is analyzed in a half-cell assembly against Li. Furthermore, the material's suitability as an intercalation-based battery-type anode in the LIC assembly is also investigated by coupling it with an AC cathode. The effect of prelithiation and different temperature conditions on the electrochemical performance of such LICs is also discussed in detail.

II. EXPERIMENT

A. Synthesis of MoO_2 nanomaterial

MoO_2 is synthesized by scalable solid-state carbothermal reduction of commercial MoO_3 [molybdenum (VI) oxide, Sigma-Aldrich, ACS reagent, ≥99.5%, molecular wt 143.94 g/mol] with carbon black (acetylene black). MoO_3 powder is thoroughly mixed with carbon black in a molar ratio (C:MoO_3) of 2.8 in a mortar and pestle, agate, for 30 min. For the reduction of MoO_3 to MoO_2, the mixture is heated from room temperature to 650 °C with a ramp of 5 °C min^{-1} under a flow of Ar and a steady temperature is maintained for 4 h. The obtained MoO_2 nanoparticle (MoO_2-np) is directly used as an electrode material.

B. Material characterization

The morphology, crystallinity, and surface chemistry of MoO_2 nanoparticles are analyzed by different analytical tools. The materials' particle morphology and surface microstructure are observed under scanning electron microscopy (SEM S-4700, Hitachi, Japan) and high-resolution transmission electron microscopy (HRTEM, JEM-2000, EX-II, JEOL, Japan). Elemental analysis is performed using energy-dispersive x-ray spectroscopy (EDS). The crystallinity and structural properties of the material samples are tested using the x-ray diffraction (XRD) technique [ULTIMA-IV, Rigaku with D/teX Ultra

250 detectors (K-β filter) through a scan speed of 0.5°/min at a step width of 0.01° for 5–90° scan range] and Raman spectroscopy using a 515-nm diode laser as an excitation light source (LabRam HR 800 UV Raman microscope, Horiba Jobin-Yvon, France). The elemental composition and surface functional groups are studied using x-ray photoelectron spectroscopy (XPS, Multilab 2000, UK; monochromatic Al $K\alpha$ radiation $h\nu = 1486.6$ eV). Thermogravimetric analysis (NETZSCH STA 449F3) is performed to understand the material's carbon content and temperature sensitivity.

C. Cell assembly and electrochemical performance analysis

The MoO_2 electrode materials are mixed with conductive carbon (acetylene black) and polyvinylidene fluoride binder in a ratio of 80:10:10 using the solvent N-methyl pyrrolidone. The obtained slurry is subjected to constant stirring, and then it is coated on Al foil using a doctor blade (MSK-AFA-III automatic thick-film coater, MTI Corporation). After drying the slurry-coated Al foils in a hot-air oven, they are pressed under a hot roll press (Tester Sangyo, Japan). 14-mm-diameter disk electrodes are punched out using an electrode cutter. AC (YP-80F, Kuraray, Japan) is considered as the active material for the capacitive-type cathode half-cell. AC electrodes are made with the help of an agate mortar and pestle. AC, conductive carbon (acetylene black), and teflonized acetylene black (TAB-2) binder are mixed in a ratio of 80 : 10 : 10 with ethanol to form a thin layer of the electrode, which is further pressed on a 14-mm stainless-steel mesh current collector (Goodfellow, UK). Before cell assembly, both the electrodes are vacuum dried for 4 h, and the half-cells are assembled using CR 2016 coin cells in an argon- (Ar) filled glovebox using 1 M $LiPF_6$ in ethylene carbonate and dimethyl carbonate (1:1 v/v) electrolyte and Whatman paper (1825-047) separator, in which Li metal serves as the counter and reference electrode. LICs are assembled by pairing both prelithiated and bare MoO_2 electrodes with AC electrodes of balanced mass. Prelithiation of MoO_2-based half-cells is performed in a half-cell assembly. The electrochemical performance of assembled half-cells and LICs is studied with a battery tester, BCS 805 (Biologic, France). Different techniques, such as electrochemical impedance spectroscopy, galvanostatic charge-discharge, and cyclic voltammetry, are used to analyze the performance of half-cells and LICs. The temperature sensitivity of the assembled LICs is tested by placing the cells inside an environmental chamber (Espec, Japan).

III. RESULTS AND DISCUSSION

MoO_2 (s) nanomaterial is prepared by reducing MoO_3 using carbon black as a reducing agent. Small in size and prominent in the number of carbon-black particles could provide numerous nucleation sites for MoO_2 formation. The molybdenum source from MoO_3 (s) is transported as MoO_3 (g) by the chemical vapor transport mechanism to the nearby carbon-black particle (nucleation sites) and is further reduced to MoO_2:

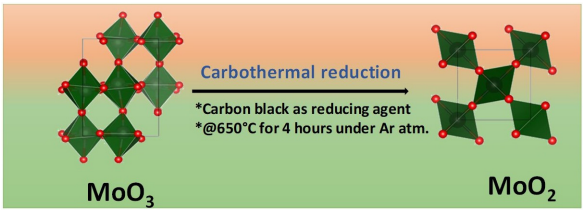

FIG. 1. Synthesis method of MoO_2-C.

$$3MoO_3(s) = (MoO_3)_3(g), \quad (3)$$

$$3MoO_3(g) + 1.5C = 3MoO_2 + 1.5CO_2. \quad (4)$$

The molar ratio of C:MoO_3 is kept at 2.8, which is more than the required ratio. It was reported that an increased number of carbon-black particles could increase the number of MoO_2 nuclei, which leads to the decreased size of MoO_2-nps [41–43]. The presence of carbon residue acts as a carbon support for the material; hence, we name it MoO_2 carbon composite (MoO_2-C). Figure 1 illustrates the synthesis method of MoO_2-C.

A. Physiochemical characterization of material

The XRD pattern of as-synthesized MoO_2-C is shown in Fig. 2(a). All the diffraction peaks in the sample are well matched with standard MoO_2 (tugarinovite, syn., with space group 14, $P121/c1$, DB number 01-074-7913, with lattice parameters $a = 5.6041$ Å, $b = 4.8550$ Å, $c = 5.6219$ Å, $\alpha = 90°$, $\beta = 120.93°$ and $\gamma = 90°$) indicating the formation of phase-pure monoclinic MoO_2 with a disordered rutile structure [28,33,44,45]. Using the Scherrer equation, the average crystallite size is determined to be 39.73 nm, which is based on the highest peaks at $2\theta = 25.97°$, corresponding to the (011) plane and by assuming spherical cubic crystallites. The absence of extra intense peaks in the XRD spectrum indicates that the residual carbon black is still in an amorphous state. Figure 2(b) illustrates the Raman spectrum of the material, showing peaks corresponding to both MoO_2 and carbon modes, indicating that the material is a carbon composite. The peaks obtained at wave numbers of 999, 826, 663, 344, and 289 cm^{-1} correspond to Raman bands of monoclinic MoO_2. The peaks at 999 and 826 cm^{-1} represent Mo-O stretching vibrations, and the peaks at 663, 344, and 289 cm^{-1} are attributed to O-Mo-O stretching, bending, and wagging, respectively [46,47]. The Raman bands positioned at 1345 and 1594 cm^{-1} correspond to the

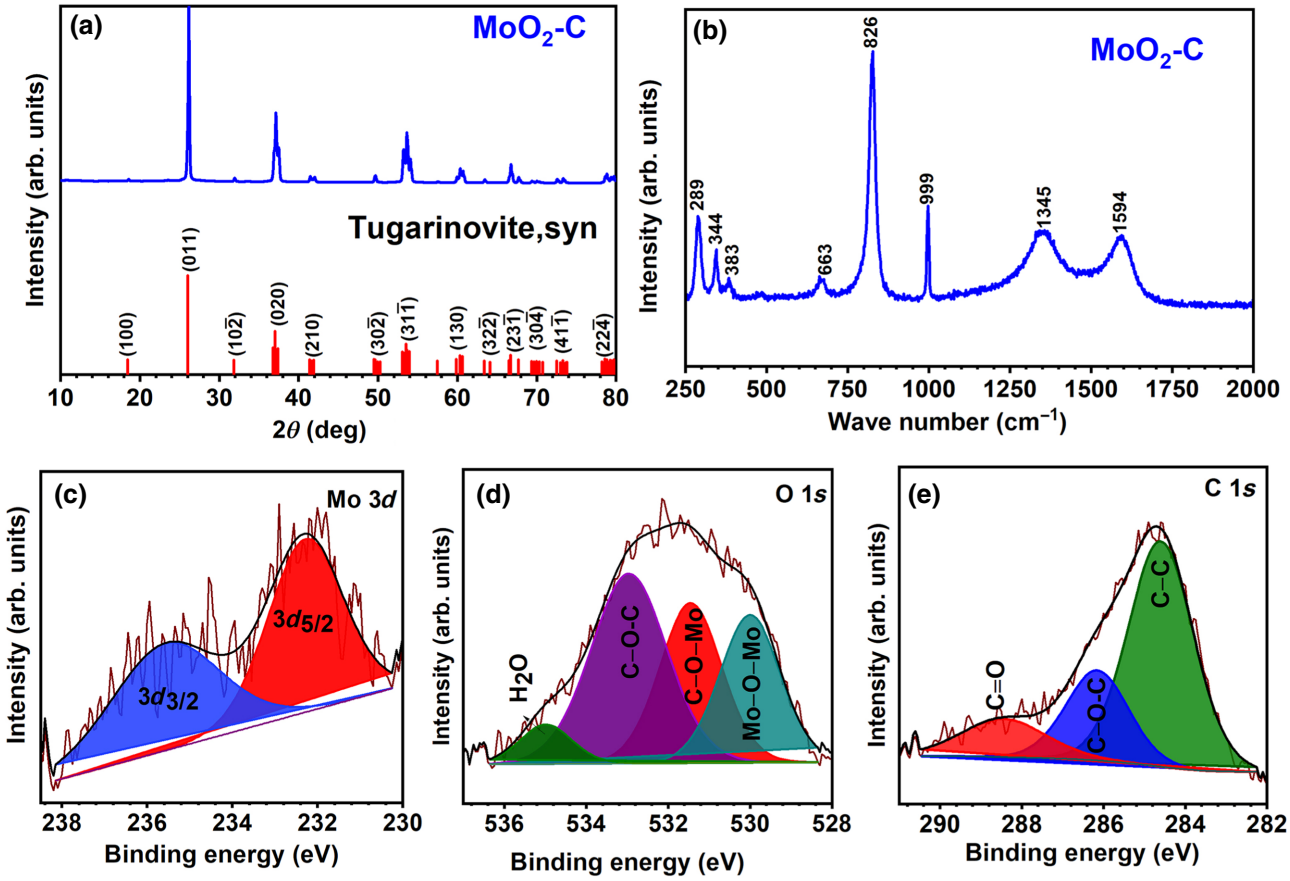

FIG. 2. (a) Powder XRD pattern; (b) Raman spectrum; high-resolution XPS spectra of (c) Mo 3*d*, (d) O 1*s*, and (e) C 1*s* of MoO_2 carbon composite.

characteristic *D* and *G* bands with an I_D/I_G value of 1.007, indicating the low degree of graphitization of amorphous carbon black [48]. The raw XPS spectrum (see the Supplemental Material [49]) shows distinct peaks at 284.6, 531.33, 231.33, and 234.17 eV, corresponding to C 1*s*, O 1*s*, Mo $3d_{5/2}$, and Mo $3d_{3/2}$, respectively, indicating the presence of carbon (C), oxygen (O), and molybdenum (Mo) elements. The peaks for Mo at 231.33 and 234.14 eV can be assigned to Mo $3d_{5/2}$ and Mo $3d_{3/2}$ of Mo^{4+}, respectively, Fig. 2(c) [50,51]. The O 1*s* peak can be deconvoluted into four peaks at 531.45, 532.96, 530, and 534.99 eV, corresponding to C-O-Mo, C-O-C, Mo-O-Mo, and chemisorbed water or weakly adsorbed oxygen molecules, respectively, Fig. 2(d). The high-energy deconvolution spectrum of the C 1*s* peak in Fig. 2(e) shows three different peaks positioned at 284.6, 286.16, and 288.46 eV attributed to C-C, C-O-C, and C–O, respectively [28,52].

Figures 3(a) and 3(b) display the field-emission (FE) SEM images of MoO_2-nps, illustrating the morphology and size of individual particles. The FESEM image in Fig. 3(b) indicates that the nanorod-shaped MoO_2 particles are randomly distributed between semispherical carbon-black particles. MoO_2 nanorods have an average diameter of 50–90 nm and a length of 100–250 nm. The carbon-black particles with an average diameter of 20 nm attach together to form aggregates and agglomerates. The surface elemental composition and elemental mapping of the particles are given in the Supplemental Material [49]. The TEM image of the particles in Fig. 3(c) indicates that the particles overlap and have a near-circular cross section. The HRTEM image in Fig. 3(d) shows lattice fringes with a *d* spacing of 3.41 nm, corresponding to the (011) plane. The high-angle annular dark field (HAADF) STEM image given in Fig. 3(e) offers atomic level resolution of the particle image. Moreover, the EDS elemental mapping of individual particles in Fig. 3(f) shows the presence of Mo, O, and C, indicating the carbon-composite nature of the MoO_2 material. Thermogravimetric analysis (TGA), Fig. 4, is carried out to determine the carbon content of the MoO_2-C sample. It is observed that there is a weight gain of about 11% above 400 °C, indicating the reformation of MoO_3 from the MoO_2 sample. This is in good agreement with the theoretical value of 12.5% weight gain for MoO_2 to MoO_3 conversion [52,53]. Above 550 °C, we can also observe a sample weight loss of 91.5 wt %, corresponding to about 20 wt % carbon content when considering weight

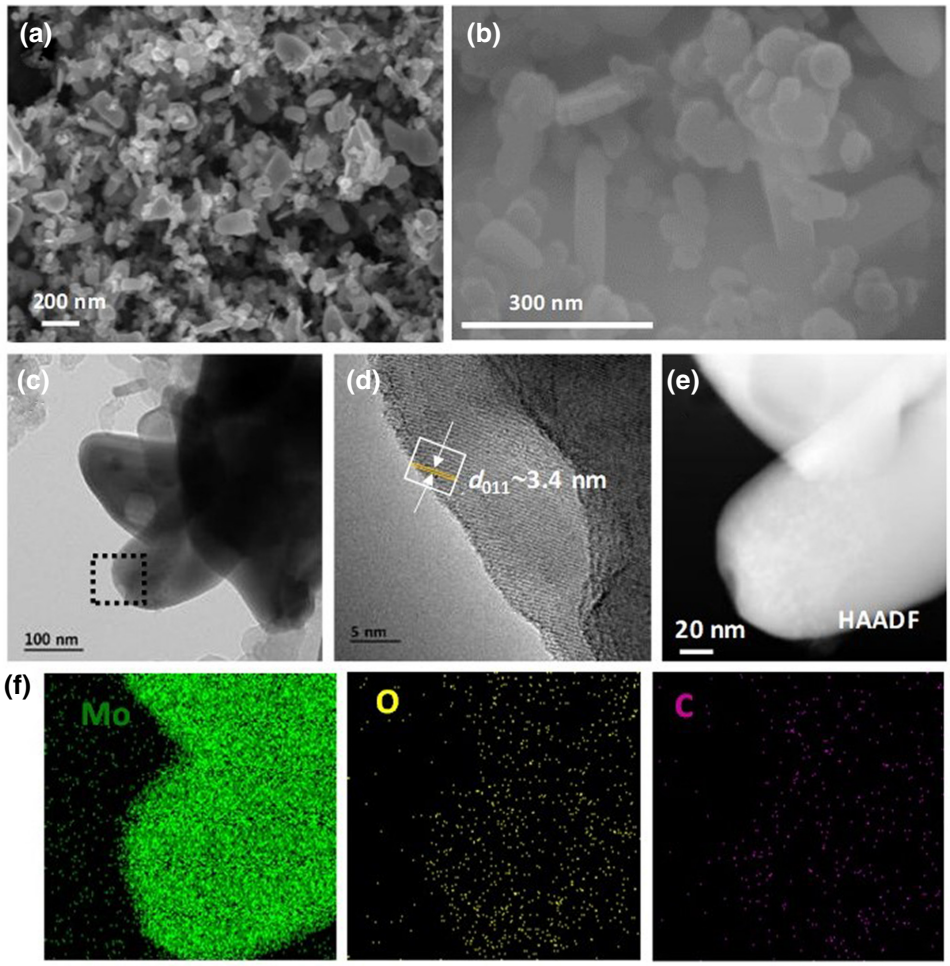

FIG. 3. (a),(b) FESEM pictures of MoO_2-C at different magnifications; (c) TEM image; (d) high-resolution TEM, (e) HAADF STEM, and (f) EDS elemental mapping images for Mo, O, and C of MoO_2 carbon composite.

gain due to oxidation; this weight loss represents the burning of residual carbon black in the sample to form CO_2 [54].

B. Electrochemical characterization

The electrochemical performance of MoO_2 nanorod carbon-composite material as an intercalation anode is tested in a half-cell assembly with a Li metal counter and reference electrode. Previous studies reported that monoclinic MoO_2 had a twisted rutile structure formed by MoO_6 octahedra arranged in the 1D tunnel structure, which facilitated reversible intercalation (deintercalation) of Li ions [37,55,56]. Most of the earlier studies reported the performance of MoO_2 as a conversion-type anode for LIB assembly [35,57]. To investigate the Li-intercalation-based storage mechanism, the potential window of the assembled half-cells is limited to between 3.0 and 0.8 V vs Li^+/Li, which avoids metallic reduction (Mo^0), i.e., the conversion reaction. Moreover, electrolyte decomposition accompanied by solid-electrolyte interface formation and other unwanted side reactions that are predominant in low-potential regions can be sidestepped. A cyclic voltammetry (CV) study is performed at different scan rates within the potential window between 0.8 and 3.0 V vs Li^+/Li. Figure 5(a) provides the first four cycles of CV profiles recorded at a scan rate of 0.1 mV s^{-1}. During the first lithiation step, four peaks can be seen at 1.7, 1.46, 1.34, and 1.17 V vs Li^+/Li. During the first delithiation step, two different peaks are observed at 1.49 and 1.7 V vs Li^+/Li. These peaks correspond to changes in ionization potentials of monoclinic and orthorhombic crystalline structures of MoO_2 nanorods. From the second cycle onwards, the cathodic peak positions are slightly shifted, such as 1.73, 1.54, 1.3, and 1.17 V vs Li^+/Li, whereas the anodic peak positions remain the same. The peaks that appear at 1.49 and 1.7 V vs Li^+/Li can be attributed to the ionization-potential change of monoclinic to orthorhombic and orthorhombic to monoclinic structures, respectively [32,37,58].

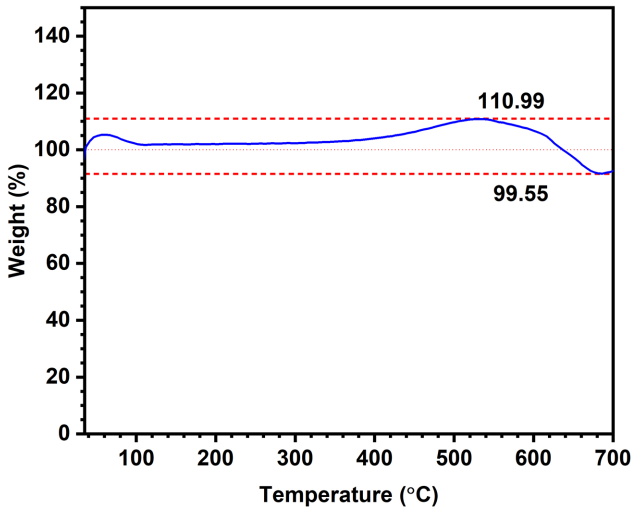

FIG. 4. TGA curve of MoO_2-C sample.

The rate capability of the material is tested at different current rates between 0.05 and 2 A g^{-1}, and we can observe that the material shows a stable performance at all the current rates tested, with a discharge capacity of about 103–107 mAh g^{-1} at 2 A g^{-1}, Figs. 5(b) and 5(c). Figure 5(d) demonstrates the galvanostatic charge-discharge (GCD) profile or voltage profile of Li/MoO_2 half-cells at a current density of 100 mA g^{-1}. It is well established that a four-step Li-intercalation reaction with two flat and two sloping plateaus is observed during intercalation (discharge profile). Whereas during deintercalation (charge profile), two near-flat plateaus are observed. This indicates reversible phase transformation from monoclinic to orthorhombic and then to monoclinic during lithiation and delithiation. The material exhibits initial discharge charge capacities of about 225–250 and 190–225 mAh g^{-1} at a current input of 100 mA g^{-1}, which is higher than the theoretical capacity of 209 mAh g^{-1}. In addition, the material exhibits good cyclic stability, with a discharge capacity of about 144 mAh g^{-1} and nearly >99% coulombic efficiency (CE), even after 500 GCD cycles, Fig. 5(e).

To further investigate the Li-intercalation mechanism in MoO_2-C nanostructures, the CV profile is recorded at different scan rates from 0.1 to 1 mV s^{-1} (see the Supplemental Material [49]). The cathodic and anodic peaks at higher scan rates are in good agreement with the CV profile at 0.1 mV s^{-1}. However, larger peak currents are obtained for fast scan rates. The pseudocapacitance contribution in the total charge-storage mechanism of the electrode material is analyzed using the power-law equation, $i = av^b$, which shows the relationship between scan rate (v) and response current (i). The constant terms a and b are adjustable parameters, and the value of b can be determined from the slope of the graph plotted between log i and log v. Based on the value of b, the mechanism of charge storage or kinetic information regarding the electrode reaction can be analyzed. The b value calculated for all four major peaks is in the range of $0.35 < b < 0.75$ (see the Supplemental Material [49]), demonstrating that the contribution from pseudocapacitance is negligible and diffusion-controlled battery-type ion intercalation (deintercalation) in the MoO_2 electrode is dominant in the overall charge-storage mechanism of the electrode material [59,60].

Additionally, electrochemical impedance spectroscopy (EIS) testing is done for the Li/MoO_2 half-cell assembly. The Nyquist plot recorded within the frequency range of 10 kHz to 1 Hz, which includes a high-to-medium-frequency semicircle, representing solution resistance (R_1), charge-transfer resistance (R_2 and R_3), constant-phase element (Q_3), and a low-frequency tail corresponding to Warburg diffusion (W_4) (see the Supplemental Material [49]). The solution resistance and charge-transfer resistance are in the range of about 15 and 55 Ω, respectively. The solid-state Li^+ diffusion coefficient from the Warburg tail is calculated to be 4.83×10^{-13} cm^2 s^{-1}, which agrees with the reported diffusion coefficient values [61–63].

Activated carbon (AC) is considered as an active cathode material in the half-cell assembly owing to its large specific surface area and porous nature; assembled Li/AC cathode half-cells display an open circuit voltage (OCV) of about 3.00–3.10 V vs Li^+/Li and are tested within the potential window of 3–4.5 V vs Li^+/Li at a current density of 100 mA g^{-1}. The cells exhibit a discharge capacity of about 50 mAh g^{-1} with nearly 100% capacity retention, even after 400 charge-discharge cycles along with >99.9% CE (see the Supplemental Material [49]). During this potential range, the electric double layer formed on the surface of the AC electrode stores PF_6^- ions. This capacitive charge-storage mechanism is also confirmed from the near-rectangular CV profile attained for the electrode (see the Supplemental Material [49]).

C. LIC assembly

We assemble LIC coin-cell (CR2016) prototypes using the MoO_2 electrode as the anode and the AC electrode as the cathode using the same electrolyte-separator system. Mass balancing is done to equalize the charge of the anode and cathode by using an anode-to-cathode mass ratio of 1 : 4. Initially, we use a prelithiated MoO_2 electrode as the anode due to the absence of Li content in both the electrode materials. The thus-formed AC//MoO_2-C LICs with an OCV of about 1.59 V are tested within the potential window of 1.7–3.2 V, considering the high Li-intercalation potential of the MoO_2 anode. Such a LIC prototype is tested at different current rates (0.01–2 A g^{-1}), and it works well at all the rates considered, with a near-linear GCD

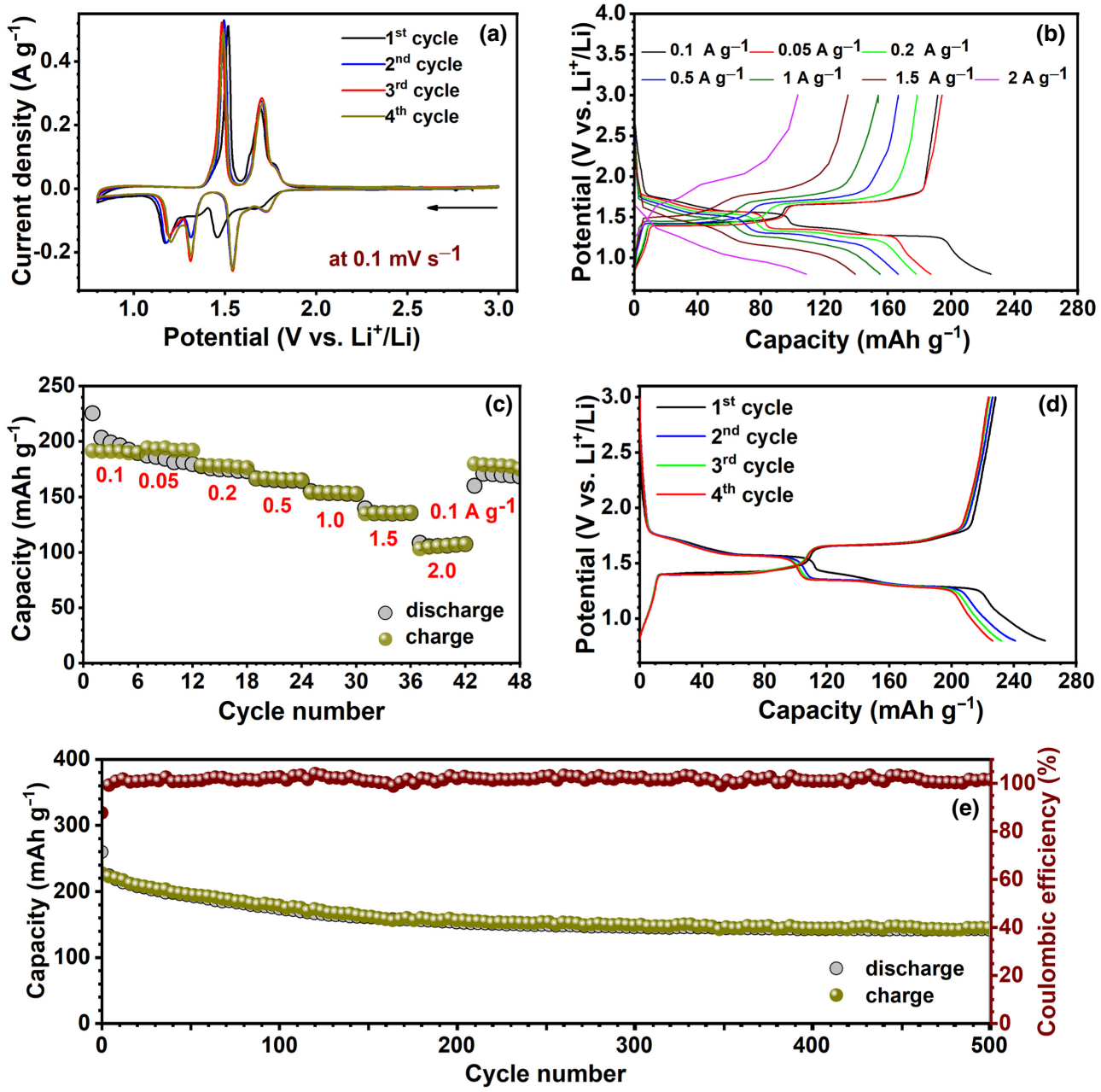

FIG. 5. Half-cell electrochemical performance of MoO_2-C anode. (a) CV profile of first four cycles recorded at a scan rate of 0.1 mV s^{-1}. (b) Charge-discharge profile at different current rates. (c) Rate performance of Li/MoO_2-C half-cell. (d) Voltage profile of first four cycles recorded at a current density of 100 mA g^{-1}. (e) Cycling performance at a current density of 100 mA g^{-1}.

profile, and it can also exhibit a maximum energy density of about 30.62 Wh kg^{-1} with a power capability of 22.35 W kg^{-1} at a current density of 0.01 A g^{-1}. At a high current rate of 1 A g^{-1}, the LIC can offer cyclic stability with about 85% capacity retention after 4500 charge-discharge cycles. To improve the energy density (calculated based on the total mass of active material in both the anode and cathode), we also test the as-formed LIC over a wide voltage window of 0.8–3.8 V. The increased potential window in the device prototype can deliver a maximum energy density of about 52.37 Wh kg^{-1} with the same power capability (22.3 W kg^{-1}). In contrast, operating the LIC device by charging and discharging to high and low potential values results in uneven capacity retention throughout the cyclic profile, mainly due to large polarization and only about 60% of the initial capacity values are maintained after 4500 cycles at a current density of 1 A g^{-1}.

Being a competitor for $Li_4Ti_5O_{12}$ (LTO), with high electrical potential (1.5 V vs Li^+/Li) and excellent safety, scientific research on MoO_2 as an intercalation-based

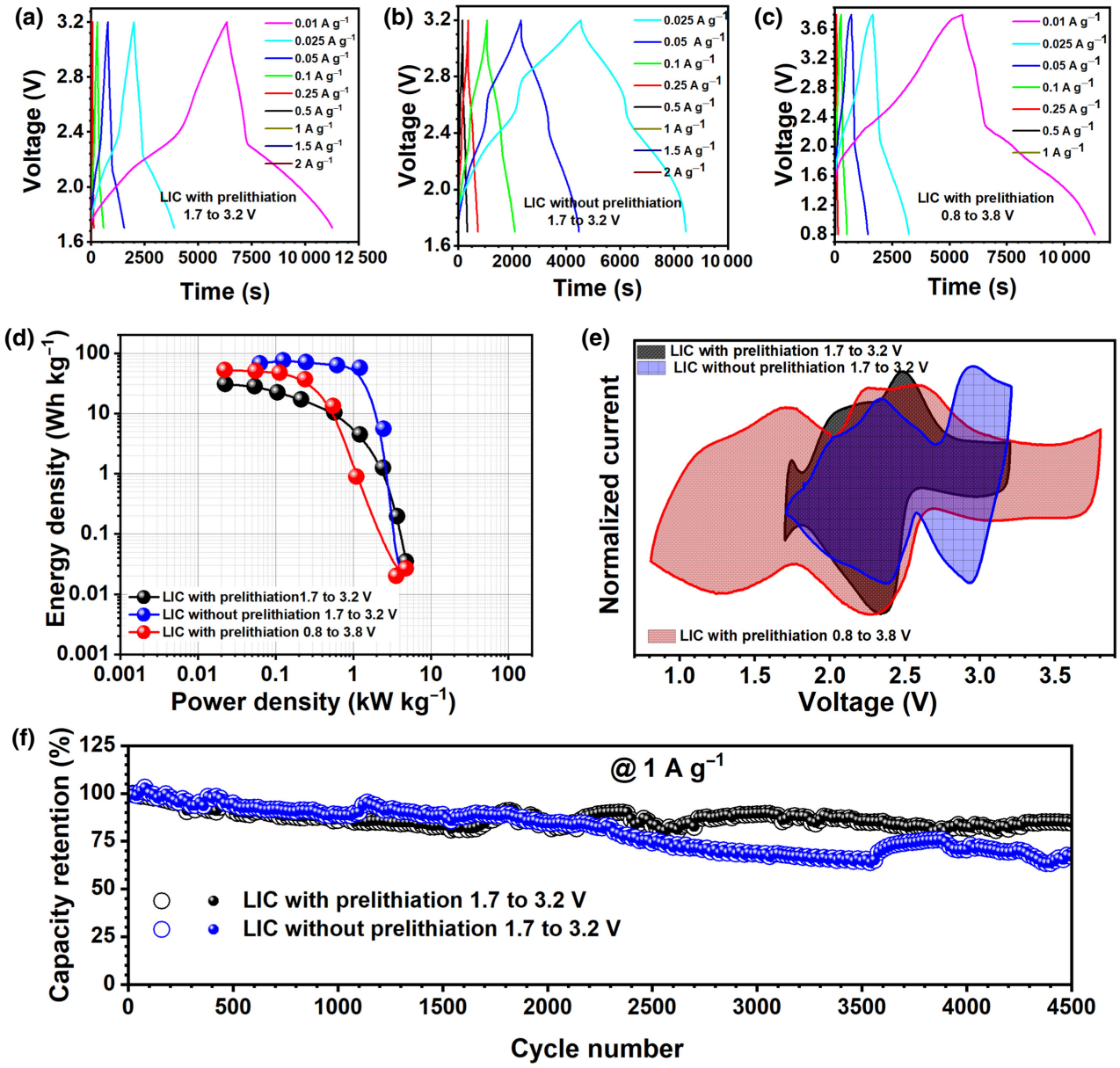

FIG. 6. Electrochemical performance of MoO_2-C anode in AC//MoO_2-C LIC assembly. (a)–(c) Typical galvanostatic charge-discharge curves at different current rates. (d) Ragone plots of LICs. (e) CV profiles at a scan rate of 1 mV s^{-1}. (f) Long-term cyclic stability of LICs when tested at a current density of 1 A g^{-1}.

battery-type anode is very significant for the future of hybrid energy-storage systems. The prelithiation strategy in the LTO-based LIC is a trending research topic, as there is still a dilemma whether prelithiation is required for LTO-based LIC assembly or not. Keeping this fact in mind, we also assemble MoO_2-based LICs without prelithiation. The LICs, thus formed, display an OCV of about 100–125 mV. When tested at different current rates, the obtained GCD profile is slightly different (isosceles triangle with a large area), indicating effective utilization of the voltage window compared to LICs assembled with a prelithiated anode. Such LICs, when operated within the voltage window of 1.7–3.2 V, can provide a maximum energy-storage capability of about 75.27 Wh kg^{-1} with a power rate of 126 W kg^{-1}. Moreover, such a LIC can also exhibit an energy-power-balanced performance of 57.07 Wh kg^{-1} at 1.22 kW kg^{-1}, indicating the actual concept of the hybrid energy-storage system. The long-term cyclability of such LICs is also tested, and we find that about 70% of the initial capacity is retained after 4500 cycles, which is slightly reduced compared to LICs with prelithiation. In addition, when these LICs without a prelithiated anode are tested under a higher voltage window of 0.8–3.8 V, they can provide a maximum energy density

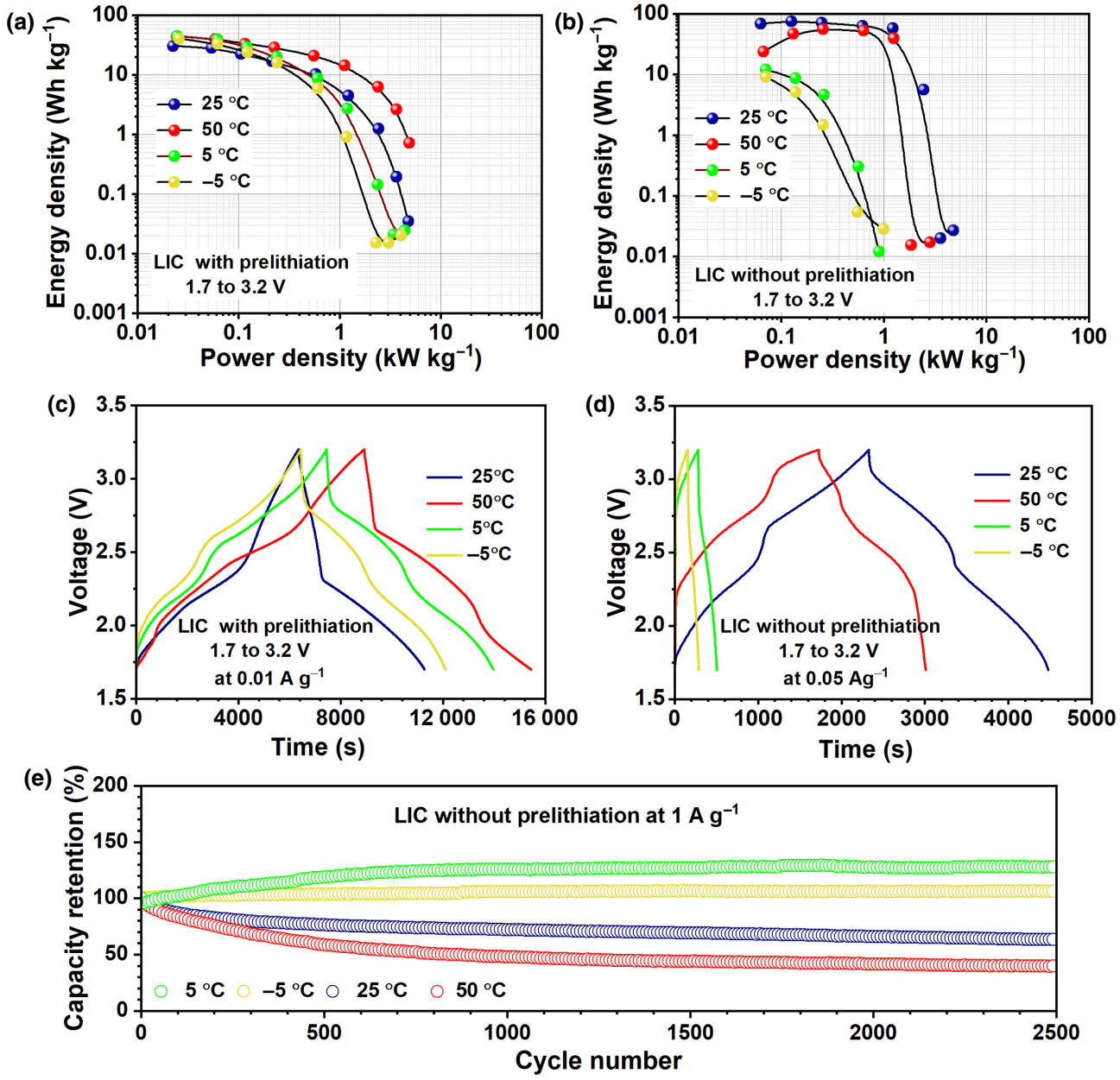

FIG. 7. Effect of temperature on electrochemical performance of AC//MoO_2-C LICs. (a),(b) Ragone plots of LICs with and without prelithiation. (c),(d) Typical galvanostatic charge-discharge profiles at a particular current rate. (e) Long-term cyclability of LIC without prelithiation at a current density of 1 A g^{-1}.

of 83.5 Wh kg^{-1} with a power density of 637 W kg^{-1}. In addition, we can also observe a balanced performance of 78.61 Wh kg^{-1} at 2.45 kW kg^{-1} with a higher current input of 1 A g^{-1}. However, these LICs are not capable of cycling for long-term performance. Figure 6 illustrates the electrochemical performance of all four LIC prototypes (see the Supplemental Material [49]).

D. Effect of temperature on LIC assembly

The wide temperature range application of hybrid capacitors still remains a significant barrier, mainly due to the meager electric conductivity of battery-type TMOs [64]. It was reported that at room temperature MoO_2 could exhibit a maximum electrical conductivity of about 11×10^5 S m^{-1} [65]. To further investigate the influence of temperature on the performance of MoO_2-based LICs, constructed LICs (with and without prelithiation having a testing voltage window limited to 1.7–3.2 V) were placed inside the environmental chamber at different low- and high-temperature conditions (−5, 5, 25, and 50 °C). The rate performance of LICs with and without prelithiation is tested at different current rates within the safe voltage

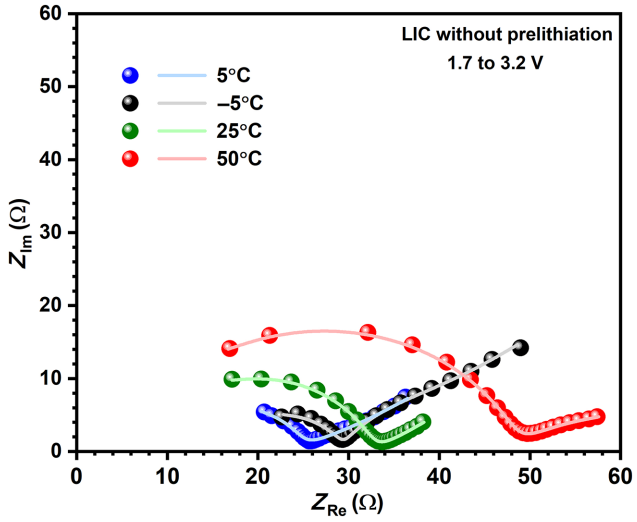

FIG. 8. EIS Nyquist plot of assembled LICs without prelithiation (1.7–3.2 V vs Li^+/Li) under different temperature conditions.

window of 1.7–3.2 V. We observe that LICs with prelithiation can deliver a stable performance at all the tested temperatures, Fig. 7(a), whereas LICs without prelithiation exhibit a slightly poor CE, mainly at low rates, when tested under high-temperature conditions, Figs. 7(b) and 7(d) (see the Supplemental Material [49]). It is observed that the cells exhibit a low rate capability; after testing at low currents, the cells do not work under high current rates. To further understand the cyclic stability of such LICs (without prelithiation) under different temperature conditions, a fresh LIC is tested at 1 $A\,g^{-1}$ for 2500 cycles at 5, –5, 25, and 50 °C, and the cells exhibit more than 100% capacity retention at 5 and –5 °C, about 65% at 25 °C, and about 42% at 50 °C, Fig. 7(e). It is observed that, under low-temperature conditions, the LIC can provide a higher capacity retention with a low energy-storage capability. Whereas, at high temperatures, the assembled LIC can store almost the same energy as that under ambient conditions but with lower capacity retention. The LIC's low energy-storage capability at low temperatures can be attributed to the reduced ionic conductivity of electrolytes and increased internal resistance of the device, whereas the increased capacity fading at high temperature could be due to accelerated active-material degradation and the increased self-discharge of the LIC system at elevated temperatures. The GCD profile of the LIC during cycling at a current density of 1 $A\,g^{-1}$ for all temperature conditions tested is given in the Supplemental Material [49]. Low energy-storage and power capabilities at low temperatures are seen in the fast charge-discharge rate of the LIC. The EIS Nyquist plot recorded for LICs within the frequency range of 10 kHz to 1 Hz shows increased charge-transfer resistance at 50 °C, which explains the increased capacity fading at elevated temperatures, Fig. 8.

IV. CONCLUSION

MoO_2-C material is synthesized by the carbothermal reduction of MoO_3. The material exhibits excellent performance (high capacity, cyclic stability, and rate capability) as an intercalation-type anode in a Li-based half-cell assembly. LICs are devised by coupling MoO_2-C as an anode with an AC cathode in a mass ratio of 1 : 4 (anode : cathode) to balance the charge. The LIC, AC//MoO_2-C assembled with a prelithiated MoO_2 anode within the voltage window of 1.7 to 3.2 V, can provide a maximum energy density of about 30.62 $Wh\,kg^{-1}$ and about 85% capacity retention after 4500 cycles under ambient temperature conditions. Avoiding the step of prelithiation and increasing the voltage window of the LIC systems results in a high energy density of about 83.5 $Wh\,kg^{-1}$ with 637 $W\,kg^{-1}$ power density. We can observe that the prelithiation step slightly lowers the energy-storage capability of the LIC system. In contrast, it can provide the LIC system's rate capability and cyclic stability. Increased voltage windows strongly disturb the cyclic stability of the system. However, we notice that LICs tested within the range of 1.7–3.2 V without prelithiation can deliver an energy density of about 75.27 $Wh\,kg^{-1}$ with a power rate of 126 $W\,kg^{-1}$ and can maintain about 70% of its initial capacity after 4500 charge-discharge cycles. Hence, such a LIC system can be considered a capable energy-storage system and can be measured as a real contender for LTO-based LIC assembly.

ACKNOWLEDGMENTS

M.L.D. is grateful for funding through the Women Scientist Scheme-B (Grant No. DST/WOS-B/2018/2039) from the KIRAN division of the Department of Science & Technology (DST), Government of India. Y.S.L. acknowledges financial support from the National Research Foundation of Korea (NRF) grant funded by the Korean Government (Ministry of Science, ICT&Future Planning) (Grant No. 2019R1-A2C1007620). V.A. acknowledges financial support from the Science and Engineering Research Board, a statutory body of the DST, Government of India, through a Start-up Research Grant (Grant No. SRG/2020/000002) and a Swarnajayanti Fellowship (Grant No. SB/SJF/2020-21/12).

CONFLICTS OF INTEREST

There are no conflicts to declare.

[1] J. Lamb and O. Burheim, Lithium-ion capacitors: A review of design and active materials, Energies **14**, 979 (2021).
[2] M. L. Divya and V. Aravindan, Electrochemically generated γ-$Li_xV_2O_5$ as insertion host for high-energy Li-ion capacitors, Chem. Asian J. **14**, 4665 (2019).

[3] S. Kasap, I. I. Kaya, S. Repp, and E. Erdem, Superbat: Battery-like supercapacitor utilized by graphene foam and zinc oxide (ZnO) electrodes induced by structural defects, Nanoscale Adv. **1**, 2586 (2019).

[4] M. Buldu-Akturk, M. Toufani, A. Tufani, and E. Erdem, ZnO and reduced graphene oxide electrodes for all-in-one supercapacitor devices, Nanoscale **14**, 3269 (2022).

[5] M. L. Divya, S. Praneetha, Y.-S. Lee, and V. Aravindan, Next-generation Li-ion capacitor with high energy and high power by limiting alloying-intercalation process using SnO_2@graphite composite as battery type electrode, Compos. B. Eng. **230**, 109487 (2022).

[6] S. Y. Lai, C. Cavallo, M. E. Abdelhamid, F. Lou, and A. Y. Koposov, Advanced and emerging negative electrodes for Li-ion capacitors: Pragmatism vs. performance, Energies **14**, 3010 (2021).

[7] V. Aravindan and Y.-S. Lee, Building next-generation Li-ion capacitors with high energy: An approach beyond intercalation, J. Phys. Chem. Lett. **9**, 3946 (2018).

[8] R. C. Massé, C. Liu, Y. Li, L. Mai, and G. Cao, Energy storage through intercalation reactions: Electrodes for rechargeable batteries, Nat. Sci. Rev. **4**, 26 (2017).

[9] L. Wang, J. Światowska, S. Dai, M. Cao, Z. Zhong, Y. Shen, and M. Wang, Promises and challenges of alloy-type and conversion-type anode materials for sodium–ion batteries, Mater. Today Energy **11**, 46 (2019).

[10] V. Aravindan, J. Gnanaraj, Y.-S. Lee, and S. Madhavi, Insertion-type electrodes for nonaqueous Li-ion capacitors, Chem. Rev. **114**, 11619 (2014).

[11] M. Li, J. Lu, X. Ji, Y. Li, Y. Shao, Z. Chen, C. Zhong, and K. Amine, Design strategies for nonaqueous multivalent-ion and monovalent-ion battery anodes, Nat. Rev. Mater. **5**, 276 (2020).

[12] S. Natarajan, Y.-S. Lee, and V. Aravindan, Biomass-derived carbon materials as prospective electrodes for high-energy lithium- and sodium-ion capacitors, Chem. Asian J. **14**, 936 (2019).

[13] M. L. Divya, S. Natarajan, Y.-S. Lee, and V. Aravindan, Achieving high-energy dual carbon Li-ion capacitors with unique low- and high-temperature performance from spent Li-ion batteries, J. Mater. Chem. A **8**, 4950 (2020).

[14] M. L. Divya, Y.-S. Lee, and V. Aravindan, Pencil powered Faradaic electrode for lithium-ion capacitors with high energy and wide temperature operation, Batter. Supercaps **5**, e202200214 (2022).

[15] J.-M. Choi, M.-S. Kwon, M.-S. Song, S. S. Hwang, H. Kim, and S.-G. Doo, Lithium intercalation of MoO_2/C composite as anode material for lithium-ion batteries, ECS Meet. Abstr. **MA2010-02**, 397 (2010).

[16] H. B. Wu, J. S. Chen, H. H. Hng, and X. Wen Lou, Nanostructured metal oxide-based materials as advanced anodes for lithium-ion batteries, Nanoscale **4**, 2526 (2012).

[17] M. Kebede, *Metal Oxide-Based Anode Materials for Lithium-Ion Battery* (Boca Raton, CRC Press, 2020).

[18] M. L. Divya, H.-Y. Lü, Y.-S. Lee, and V. Aravindan, Prelithiated $Li_{4+x}Ti_5O_{12}$ ($0 \leq x \leq 3$) anodes towards building high-performance Li-ion capacitors, Sustain. Energy Fuels **6**, 4884 (2022).

[19] W. Qi, J. G. Shapter, Q. Wu, T. Yin, G. Gao, and D. Cui, Nanostructured anode materials for lithium-ion batteries: Principle, recent progress and future perspectives, J. Mater. Chem. A **5**, 19521 (2017).

[20] V. Pralong, Lithium intercalation into transition metal oxides: A route to generate new ordered rock salt type structure, Prog. Solid State Chem. **37**, 262 (2009).

[21] M. Mattinen, *et al.*, Atomic layer deposition of crystalline molybdenum oxide thin films and phase control by post-deposition annealing, Mater. Today Chem. **9**, 17 (2018).

[22] J. R. Dahn and W. R. McKinnon, Structure and electrochemistry of Li_xMoO_2, Solid State Ionics **23**, 1 (1987).

[23] J. Gopalakrishnan, Insertion/extraction of lithium and sodium in transition metal oxides and chalcogenides, Bull. Mater. Sci. **7**, 201 (1985).

[24] J. J. Auborn and Y. L. Barberio, Lithium intercalation cells without metallic lithium: $MoO_2/LiCoO_2$ and $WO_2/LiCoO_2$, J. Electrochem. Soc. **134**, 638 (1987).

[25] R. Tokarz-Sobieraj, R. Gryboś, and M. Witko, Electronic structure of MoO_2. DFT periodic and cluster model studies, Appl. Catal. A **391**, 137 (2011).

[26] A. Magnéli and G. Andersson, On the MoO_2 structure type, Acta Chem. Scand. **9**, 1378 (1955).

[27] I. A. de Castro, R. S. Datta, J. Z. Ou, A. Castellanos-Gomez, S. Sriram, T. Daeneke, and K. Kalantar-zadeh, Molybdenum oxides – from fundamentals to functionality, Adv. Mater. **29**, 1701619 (2017).

[28] Q. Yang, Q. Liang, J. Liu, S. Liang, S. Tang, P. Lu, and Y. Lu, Ultrafine MoO_2 nanoparticles grown on graphene sheets as anode materials for lithium-ion batteries, Mater. Lett. **127**, 32 (2014).

[29] H.-J. Zhang, Q.-C. Jia, and L.-B. Kong, Molybdenum dioxide supported carbon nanotubes@carbon constructs disordered nanocluster particles as anodes for lithium-ion capacitors with long-term cycling stability, J. Mater. Sci. **32**, 18912 (2021).

[30] X. Wang, Y. Liu, J. Zeng, C. Peng, and R. Wang, MoO_2/C hollow nanospheres synthesized by solvothermal method as anode material for lithium-ion batteries, Ionics **25**, 437 (2019).

[31] H. S. Majdi, Z. A. Latipov, V. Borisov, N. O. Yuryevna, M. M. Kadhim, W. Suksatan, I. H. Khlewee, and E. Kianfar, Nano and battery anode: A review, Nanoscale Res. Lett. **16**, 177 (2021).

[32] X. Zhang, Z. Hou, X. Li, J. Liang, Y. Zhu, and Y. Qian, MoO_2 nanoparticles as high capacity intercalation anode material for long-cycle lithium ion battery, Electrochim. Acta **213**, 416 (2016).

[33] H.-S. Kim, J. Cook, S. Tolbert, and B. Dunn, The development of pseudocapacitive properties in nanosized-MoO_2, J. Electrochem. Soc. **162**, A5083 (2015).

[34] J. Ni, Y. Zhao, L. Li, and L. Mai, Ultrathin MoO_2 nanosheets for superior lithium storage, Nano Energy **11**, 129 (2015).

[35] Y. Liu, H. Zhang, P. Ouyang, and Z. Li, One-pot hydrothermal synthesized MoO_2 with high reversible capacity for anode application in lithium ion battery, Electrochim. Acta **102**, 429 (2013).

[36] J. Li, *et al.*, Phase evolution of conversion-type electrode for lithium ion batteries, Nat. Commun. **10**, 2224 (2019).

[37] U. K. Sen, A. Shaligram, and S. Mitra, Intercalation anode material for lithium ion battery based on

molybdenum dioxide, ACS Appl. Mater. Interfaces **6**, 14311 (2014).
[38] X. Liu, J. Yang, W. Hou, J. Wang, and Y. Nuli, Highly reversible lithium-ions storage of molybdenum dioxide nanoplates for high power lithium-ion batteries, ChemSusChem **8**, 2621 (2015).
[39] A. Kim, E. Park, H. Lee, and H. Kim, Highly reversible insertion of lithium into MoO_2 as an anode material for lithium ion battery, J. Alloys Compd. **681**, 301 (2016).
[40] X. Zhao, H.-E. Wang, J. Cao, W. Cai, and J. Sui, Amorphous/crystalline hybrid MoO_2 nanosheets for high-energy lithium-ion capacitors, Chem. Commun. **53**, 10723 (2017).
[41] G.-D. Sun, G.-H. Zhang, B.-J. Yan, and K.-C. Chou, Study on the reduction of commercial MoO_3 with carbon black to prepare MoO_2 and Mo_2C nanoparticles, Int. J. Appl. Cer. Technol. **17**, 917 (2020).
[42] G.-D. Sun, G.-H. Zhang, X.-P. Ji, J.-K. Liu, H. Zhang, and K.-C. Chou, Size-controlled synthesis of nano Mo powders via reduction of commercial MoO_3 with carbon black and hydrogen, Int. J. Refract. Met. Hard Mater. **80**, 11 (2019).
[43] L. Wang, Z.-L. Xue, A. Huang, and F.-F. Wang, Mechanism and kinetic study of reducing MoO_3 to MoO_2 with CO–15 vol % CO_2 mixed gases, ACS Omega **4**, 20036 (2019).
[44] Q. Tang, Z. Shan, L. Wang, and X. Qin, MoO_2–graphene nanocomposite as anode material for lithium-ion batteries, Electrochim. Acta **79**, 148 (2012).
[45] D. Wu, R. Shen, R. Yang, W. Ji, M. Jiang, W. Ding, and L. Peng, Mixed molybdenum oxides with superior performances as an advanced anode material for lithium-ion batteries, Sci. Rep. **7**, 44697 (2017).
[46] M. Dieterle, G. Weinberg, and G. Mestl, Raman spectroscopy of molybdenum oxides Part I. Structural characterization of oxygen defects in MoO_{3-x} by DR UV/VIS, Raman spectroscopy and x-ray diffraction, Phys. Chem. Chem. Phys. **4**, 812 (2002).
[47] M. Dieterle and G. Mestl, Raman spectroscopy of molybdenum oxides Part II. Resonance Raman spectroscopic characterization of the molybdenum oxides Mo_4O_{11} and MoO_2, Phys. Chem. Chem. Phys. **4**, 822 (2002).
[48] M. Youssry, F. Z. Kamand, M. I. Magzoub, and M. S. Nasser, Aqueous dispersions of carbon black and its hybrid with carbon nanofibers, RSC Adv. **8**, 32119 (2018).
[49] See the Supplemental Material at http://link.aps.org/supplemental/10.1103/PhysRevApplied.19.034016 for the raw XPS spectrum, SEM EDS mapping results, the half-cell performance of MoO_2 and AC, the LIC performance with and without prelithiation between 0.8 and 3.8 V, and the LIC performance with prelithiation at 1.7–3.2 V at various temperature conditions and its comparison without prelithiation.
[50] J. Baltrusaitis, B. Mendoza-Sanchez, V. Fernandez, R. Veenstra, N. Dukstiene, A. Roberts, and N. Fairley, Generalized molybdenum oxide surface chemical state XPS determination via informed amorphous sample model, Appl. Surf. Sci. **326**, 151 (2015).
[51] D. O. Scanlon, G. W. Watson, D. J. Payne, G. R. Atkinson, R. G. Egdell, and D. S. L. Law, Theoretical and experimental study of the electronic structures of MoO_3 and MoO_2, J. Phys. Chem. C **114**, 4636 (2010).
[52] H. Wang, *et al.*, Nanostructured molybdenum-oxide anodes for lithium-ion batteries: An outstanding increase in capacity, Nanomaterials **12**, 13 (2022).
[53] L. Wang, G.-H. Zhang, and K.-C. Chou, Study on oxidation mechanism and kinetics of MoO_2 to MoO_3 in air atmosphere, Int. J. Refract. Met. Hard Mater. **57**, 115 (2016).
[54] Q. Tang, Z. Shan, L. Wang, and X. Qin, MoO_2-graphene nanocomposite as anode material for lithium-ion batteries, Electrochim. Acta **79**, 148 (2012).
[55] U. Sen and S. Mitra, Synthesis of molybdenum oxides and their electrochemical properties against Li, Energy Procedia **5407315**, 740 (2014).
[56] Y. Zhu, X. Ji, S. Cheng, J. Jia, H. Luo, L. Tang, T. Liu, M. Li, and M. Liu, Achieving durable and fast charge storage of MoO_2-based insertion-type pseudocapacitive electrodes via N-doped carbon coating, ACS Sustain. Chem. Eng. **8**, 2806 (2020).
[57] S. Petnikota, K. W. Teo, L. Chen, A. Sim, S. K. Marka, M. V. Reddy, V. V. S. S. Srikanth, S. Adams, and B. V. R. Chowdari, Exfoliated graphene oxide/MoO_2 composites as anode materials in lithium-ion batteries: An insight into intercalation of Li and conversion mechanism of MoO_2, ACS Appl. Mater. Interfaces **8**, 10884 (2016).
[58] X. Zhang, Z. Hou, X. Li, Y. Zhu, and Y. Qian, MoO_2 nanoparticles as high capacity intercalation anode material for long-cycle lithium ion battery, Electrochim. Acta **213**, 416 (2016).
[59] Y. Liu, S. P. Jiang, and Z. Shao, Intercalation pseudocapacitance in electrochemical energy storage: Recent advances in fundamental understanding and materials development, Mater. Today Adv. **7**, 100072 (2020).
[60] Y. Jiang and J. Liu, Definitions of pseudocapacitive materials: A brief review, Energy Environ. Mater. **2**, 30 (2019).
[61] F. Chen, *et al.*, Novel designed MnS-MoS_2 heterostructure for fast and stable Li/Na storage: Insights into the advanced mechanism attributed to phase engineering, Adv. Funct. Mater. **31**, 2007132 (2021).
[62] T. Li, M. Beidaghi, X. Xiao, L. Huang, Z. Hu, W. Sun, X. Chen, Y. Gogotsi, and J. Zhou, Ethanol reduced molybdenum trioxide for Li-ion capacitors, Nano Energy **26**, 100 (2016).
[63] V. P. Tysyachny, E. Shembel, R. Apostolova, V. M. Nagirny, and K. Kylyvnyk, Chronovoltammetry of electrolytic molybdenum oxides at the electrochemical intercalation/deintercalation of lithium ions, J. Solid State Electrochem. **8**, 20 (2003).
[64] Y. Yin, Z. Fang, J. Chen, Y. Peng, L. Zhu, C. Wang, Y. Wang, X. Dong, and Y. Xia, Hybrid Li-ion capacitor operated within an all-climate temperature range from −60 to +55 °C, ACS Appl. Mater. Interfaces **13**, 45630 (2021).
[65] F. Kaiser, M. Schmidt, Y. Grin, and I. Veremchuk, Molybdenum oxides MoO_x: Spark-plasma synthesis and thermoelectric properties at elevated temperature, Chem. Mater. **32**, 2025 (2020).